Journal Pre-proof

Net zero fuel (mixed hydrogen and biofuels) cement clinker: Characterisation, microstructure, and performance.

Samuel Adu-Amankwah, Ben Douglas, Leslie Arkless, Nina Cardinal, Maciej Zajac

PII: S0958-9465(24)00387-1

DOI: https://doi.org/10.1016/j.cemconcomp.2024.105814

Reference: CECO 105814

To appear in: *Cement and Concrete Composites*

Received Date: 12 July 2024

Revised Date: 18 October 2024

Accepted Date: 22 October 2024

Please cite this article as: S. Adu-Amankwah, B. Douglas, L. Arkless, N. Cardinal, M. Zajac, Net zero fuel (mixed hydrogen and biofuels) cement clinker: Characterisation, microstructure, and performance., *Cement and Concrete Composites*, https://doi.org/10.1016/j.cemconcomp.2024.105814.

Net zero fuel (mixed hydrogen and biofuels) cement clinker: Characterisation, microstructure, and performance.

Samuel Adu-Amankwah[1*], Ben Douglas[2], Leslie Arkless[3], Nina Cardinal[4], Maciej Zajac[5]

[1]Department of Civil Engineering, Aston University, Birmingham, B4 7ET, United Kingdom

[2]School of Chemical and Process Engineering, University of Leeds, Leeds, LS2 9JT, United Kingdom

[3]School of Chemistry, University of Leeds, Leeds, LS2 9JT, United Kingdom

[4]Heidelberg Materials UK, Global Research & Development, Cement National Technical Centre, Scunthorpe, DN16 1AW, United Kingdom

[5]Heidelberg Materials AG, Global Research & Development, Oberklamweg 2-4, 69181 Leimen, Germany

*Corresponding author: s.adu-amankwah@aston.ac.uk

Net zero fuel clinker characterisation

Hydration kinetics and phase assemblage of CEM I and GGBS blends

Performance

Clinker granules

CEM I

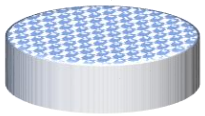

In resin

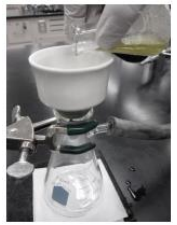

Selective dissolution

C_3S, α'-C_2S↑, β-C_2S↓, C_3A, C_4AF

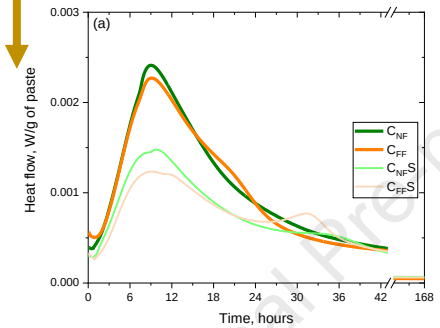

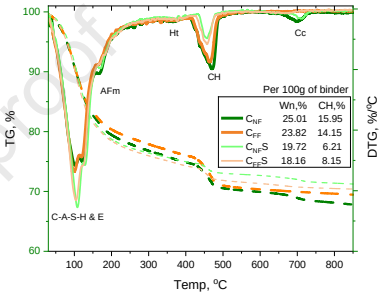

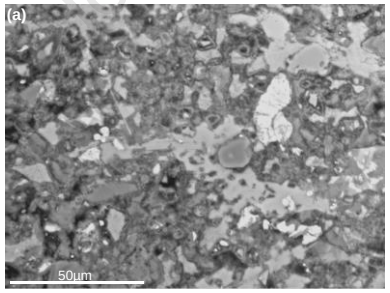

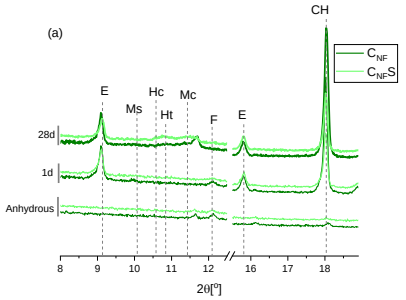

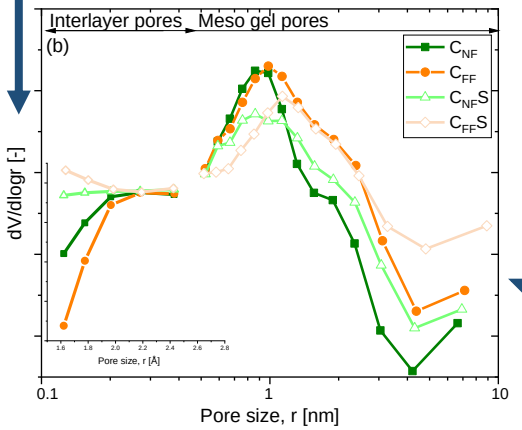

Porosity

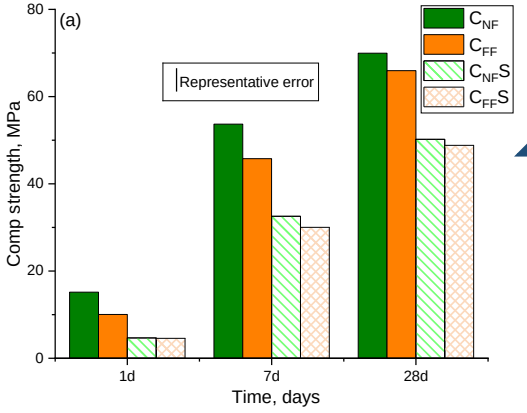

Strength

SEM NMR XRD

IC SEM TGA XRD

Net zero fuel (mixed hydrogen and biofuels) cement clinker: Characterisation, microstructure, and performance.

Abstract

Over 35% of the CO_2 associated with cement production comes from operational energy. The cement industry needs alternative fuels to meet its net zero emissions target. This study investigated the influence of hydrogen mixed with biofuels, herein designated net zero fuel as an alternative to coal, on the clinker quality and performance of cement produced in an industrial cement plant. Scanning electron microscopy, X-ray diffraction and nuclear magnetic resonance were coupled to study the clinker mineralogy and polymorphs. Hydration and microstructure development in plain and slag blended cements based on the clinker were compared to commercial cement equivalent. The results revealed a lower alite/belite ratio, but a significant proportion of the belite was of the α'_H-C_2S polymorph. These reacted faster and compensated for the alite/belite ratio. Gel and micro-capillary pores were densified, which reduced total porosity and attained comparable strength to the reference plain and blended cement. This study demonstrates that the investigated net zero fuel-produced clinker meets compositional and strength requirements for plain and blended cement, providing a feasible pathway for the cement industry to lower its operational carbon significantly.

Keywords: *Net zero fuel, Hydrogen fuel, biofuel, clinker manufacturing, hydration and microstructure*

Introduction

Concrete is the most used manufactured material. The production of cement, the binder that holds the aggregate and affords concrete its desirable properties, is energy and CO_2-intensive. Approximately 3.2 GJ energy is required to produce one tonne of cement clinker in a modern kiln [1], and the process generates 0.58 – 0.87 tCO_2e/t of cement [2]. This accounts for over 35% of the operational carbon from cement kilns, with the remaining 65% associated with the breakdown of limestone into quicklime [3], which is inherent in cement clinker manufacturing. For the cement industry to attain its 2050 emissions reduction targets, coupling approaches to lower energy-related emissions and increasing the use of alternative materials is essential.

Cement decarbonisation strategies have focused on reducing the clinker factor through increased use of supplementary cementitious materials (SCMs) [4], alternative fuels [5] and carbon capture utilisation and storage (CCUS) from the cement plant [6]. CCUS and carbon-free clinkering raw materials will be game changers, but the enabling technologies are still evolving and remain medium to long-term strategies. Meanwhile, blended cements, which reduce the clinker factor (and offset the related emissions) in concrete, have been standardized and deployed for many decades. However, slow strength evolution limits practical clinker substitution to at most 50% in most applications [4, 7]. Moreover, the closure of coal combustion power stations and the shift from blast furnaces to electric arc furnace steel production threaten the availability of suitable industrial SCMs, e.g., pulverized fuel ashes and ground granulated blast furnace slag (GGBS), putting into doubt the sustainability of emission reduction through conventional SCMs. Consequently, carbon-free fuels for clinker production will be a practical and impactful strategy towards net zero emission goals.

The energy requirements in the cement plant are traditionally met by coal, petcoke or natural gas, with air as the oxidiser. Increasingly, liquid and solid wastes with different calorific values are used in industrial cement plants as cost and environmental management strategies. Alternative fuels in the cement plant reduce the demand for fossil fuels and energy-related emissions. For example, several cement plants have utilised municipal and industrial wastes, sewage sludge, scrap tyres and biomass residues, providing 20 – 50% of the cement plants' operational energy [8, 9]. However, these fuels differ in carbon, moisture, trace elements and volatile contents, which affect their burnability [10],

modifying the kiln's temperature profile and, consequently, the clinker composition and emissions from the plant [11].

The modification of the clinker composition and the availability and cost of fuel are significant factors influencing fuel switching in the cement plant. Commonly used alternative fuels, while having lower calorific values than fossil fuels[5, 12], present unique challenges. Their use is associated with a lower heating rate and, depending on the fuel mix, can reduce the peak temperature in the kiln [5]. The effect of such changes on the clinker quality can be profound. For example, moderate reductions in the heating rate were associated with under-burning, where the clinkers were characterised by a low alite/belite ratio and more free lime [13]. Conversely, a higher heating rate increased the M_1/M_3 alite polymorphs ratio with larger alite crystals due to the dissolution of lime and belite [14]. Volatiles in the fuels also affect the clinker polymorphs. For example, phosphorus in agriculture waste and meat and bone meal (MBM) can also be incorporated into the calcium silicate minerals. This stabilises belite over alite, as reported in [15-17] and elevates the free lime content in the clinker [18]. Similarly, metals in scrapped tyres used as alternative clinkering fuel increase zinc concentration in the resulting clinkers [19]. Meanwhile, alterations in alite grain sizes and polymorphs were identified in biomass and tyre-derived fuel clinkers, which reduced reactivity [20]. Besides trace element inclusions, relationships between the cement kiln's temperature profile and the reactivity of the calcium silicate polymorphs have been reported. The alite polymorphs were shown to increase reactivity in the order $M_3 < M_1$ [21] and for belite, $\gamma < \alpha'_L < \beta < \alpha'_H < \alpha$ [22, 23]. Therefore, it is imperative to identify potential polymorphic changes in the main clinker phases arising from changes in the kiln fuel composition and, particularly, the switch to new cleaner fuels.

Hydrogen-derived fuels have attracted attention across several industries due to their high calorific value, combustibility and zero carbon intensity. Hydrogen may be generated from natural gas with or without carbon capture, classified as blue and grey hydrogen, respectively [24] or by electrolysis using renewable energy [25]. Presently, supplies to the hydrogen-intensive petroleum and agrochemical industries are met through grey sources. The feasibility of hydrogen-powered cement kilns, integration and synergies for hydrogen generation [26] and their combination with other fuels [10] have been modelled in the literature. For example, the integration of a Cu-Cl thermochemical cycle in cement works as a low-cost and low-energy alternative to water electrolysis via electrification was analysed in [27]. The regenerative loop exposed cupric chloride salts to steam to form copper oxychloride, which melted at 500°C, generating hydrogen and oxygen and recycling the chloride salt. Hydrogen from the decomposition of liquefied ammonia was analysed in [28]. A portion of the thermal energy from the kiln's reaction was used to decompose ammonia, the conversion rate of which exceeded 80% at 450°C depending on the catalyst. At the same time, the bulk composition of the resulting clinker was comparable to the coal-produced clinker except for slightly elevated alkali levels. Despite the promising hydrogen production pathways, an understanding of the impact of faster combustibility on clinker quality is lacking. A recent simulation study [10] identified potential fuel miscibility and temperature distribution issues associated with alternative cement kiln fuels including blends with hydrogen. Consequently, industrial-scale trials of such fuels and systematic assessment of the clinker produced from them are imperative to optimise fuel composition and performance.

In this study, a systematic experimental programme is followed to investigate representative clinker and cement from a recently completed net zero fuel switching (i.e., mixed hydrogen and biofuels) trial in the UK. The objective is to examine the influence of the fuel switching on the clinker minerals. Further, hydration of plain and blended slag cements based on the net zero fuel clinker is studied alongside the microstructure and strength development to elucidate underlying factors controlling performance of the cements compared to fossil fuel equivalent.

Materials and methods

Materials

A net zero fuel produced cement clinker and its corresponding CEM I 52.5 N from a recent UK fuel switching trial project [29] was characterised. The fuel comprised up to 20% hydrogen mixed with 35% glycerine and 10% MBM partially replacing coal in the cement pre-calciner and kiln. Hanson Cement UK supplied the clinker and cement.

Four cements, namely the net zero fuel CEM I 52.5 N (C_{NF}), a reference commercial grade CEM I 52.5 N (C_{FF}) and their corresponding blends with GGBS designated $C_{NF}S$ and $C_{FF}S$, respectively were investigated to assess the impact of the net zero clinkering fuel on hydration, microstructure, and strength development.

In preparing the blended cement, a 1:1 ratio was maintained between the CEM I and GGBS and the total sulphate content was adjusted to 3%. Particle size distributions of C_{NF}, C_{FF} and GGBS (S) were measured using a Malvern Panalytical Mastersizer 3000 with an Aero S air dispersion unit and standard Venturi dispenser. Values of refractive index 1.680 and absorption coefficient 0.1 were used to process the data. Three portions of each sample were analysed, and the results were averaged to produce a volume and cumulative distributions as shown in Figure 1. The Blain fineness was 492, 475 and 510 kg/m^2 for C_{NF}, C_{FF} and GGBS respectively.

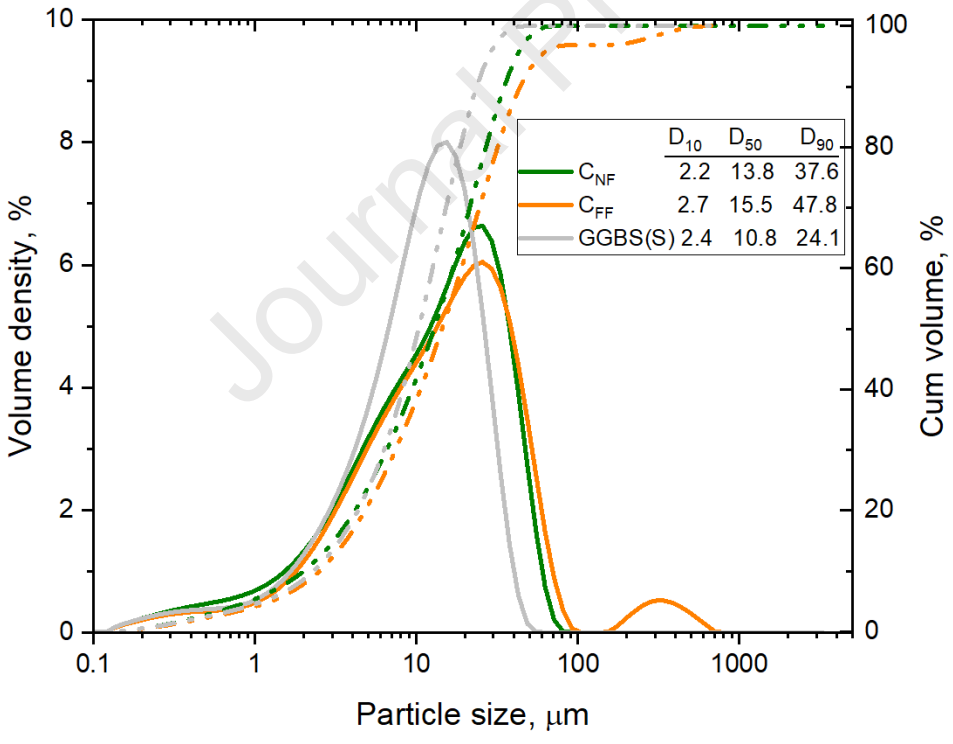

Figure 1 Particle size distribution of C_{NF}, C_{FF} and GGBS as determined by laser granulometry.

For determining the oxide compositions, the as-received cement and GGBS were initially tested for loss on ignition (LOI) at 900°C in a muffle furnace before the powders were prepared for X-ray fluorescence (XRF) using the fused bead method. The results are shown in Table 1.

Compositionally, the two cements were similar except for slightly elevated levels of alkalis in C_{NF} and higher LOI reflecting the higher limestone content than C_{FF} cement. Meanwhile, the P_2O_5 content in C_{NF} was lower than expected for clinkers made with MBM-containing fuels. However, at 10% fuel substitution with MBM, the detected 0.2% P_2O_5 was acceptable. It should also be noted that phosphorous incorporation into clinkers, a risk associated with high MBM as cement kiln fuel substitute, depends on its concentration and the feed rate [30].

Table 1 Chemical composition of C_{NF}, C_{FF} and GGBS as measured by XRF (% weight).

Material	CaO	SiO_2	Al_2O_3	Fe_2O_3	MgO	K_2O	Na_2O	SO_3	TiO_2	P_2O_5	Cl	ZnO_2	LOI
C_{NF}	63	19.5	4.9	2.1	2.3	0.6	0.3	3.5	0.2	0.2	0.07	0.03	3.3
C_{FF}	64.9	19.5	5.1	3.1	1.1	0.5	0.13	3.1	0.4	0.1	0.05	0.01	1.9
GGBS(S)	41.8	34.9	11.6	0.5	5.8	0.5	0.1	3.1	1.1	0.02	-	-	1.5

Methods

The study comprised two experimental stages:

1. Characterisation of the anhydrous net zero fuel (NF) clinker and cement.
2. Characterisation of reaction kinetics, microstructure and performance of plain and GGBS blended cement based on the net zero fuel clinker in comparison to the reference commercial cement equivalent.

Characterisation of the anhydrous net zero fuel clinker and cement

The as-received clinker was prepared for microanalysis under a scanning electron microscope (SEM), while the anhydrous cement and corresponding enriched silicate and interstitial phases were investigated using X-ray diffraction (XRD) and solid-state nuclear magnetic resonance (NMR). The procedures for selectively enriching the silicate and interstitial phases in the cements were adopted from [31]. For enriching the silicates, the cement was dissolved in potassium hydroxide and sucrose extraction solution prepared at 9:1:1 in 300 ml deionized water at 95°C. After 1 minute of stirring, the solution was vacuum filtered using an 11 µm cellulose filter paper in a Buchner funnel. The residue was washed with deionized water and methanol before drying at 60°C. Meanwhile, the interstitial phases were enriched by dissolving 5 g of the cement powder in a 1:15 salicylic acid and methanol solution before vacuum filtering and drying the residue at 90°C. The dry powders were stored in a desiccator until characterisation.

For observation under the SEM, the clinker granules were embedded in resin under vacuum and cured overnight at room temperature. After removal from the mould, the resin was polished down to 0.25 µm using silicon carbide paper and cloths with diamond paste. Images were acquired in backscattered electron mode using a Zeiss EVO 15 SEM with Lab6 filament equipped with a 150 mm^2 Oxford Instruments X-Max EDS detector controlled with the Aztec software. The instrument was operated at 15 KeV accelerating voltage. Elemental mapping and point analyses were carried out to investigate the composition of the main clinker phases, with the backscattered images and combined maps used to determine the grain sizes.

XRD data were acquired on the as-received and selectively enriched C_{FF} and C_{NF} powder samples. The objective was to identify potential differences in the polymorphs of the main clinker phases resulting from the net zero fuel. The measurements were performed on a Phillips Empyrean diffractometer using a CuKα anode operated at 45 kV and 40 mA and equipped with a PIXcel3D detector without a monochromator. The powders were backloaded into a 10 mm diameter sample holder and scanned on the PW3064 spinner stage. Data acquisition was done at 0.0131 step size with 73.6 s per step

between 5 – 80 2θ° range. Rietveld analyses of the diffraction data were conducted using the TOPAS Academic v7.21 software. A control file comprising crystallographic information files for the identified minerals, constrained, and refined on the enriched samples' data was used to quantify the crystalline phases in the anhydrous cements. The external standard method was used to determine the absolute phase contents using a 98% purity corundum standard.

Solid-state magic angle spinning (MAS) NMR measurements were performed to understand the impact of the fuel switch on the chemical environment of Al and Si. Data was acquired on a Bruker Avance III HD 400 MHz wide bore magnet (magnetic field 9.4 T) with all data acquired at 54.74° magic angle. ^{29}Si MAS NMR spectra were collected at an operating frequency of 79.48 MHz, using a zirconia rotor, and spun at 6 kHz in a 7 mm solid-state MAS probe using a 90° pulse of duration of 5.5 µs, a relaxation delay of 30 s and a minimum of 2,048 scans. ^{27}Al MAS NMR spectra were collected at an operating frequency of 104.23 MHz, using a zirconia rotor, and spun at 20 kHz in a 2.5 mm solid-state MAS probe, and employed a 90° pulse of duration 0.23 µs, a relaxation delay of 0.5 s and a minimum of 16,384 scans. Chemical shifts in the ^{29}Si and ^{27}Al spectra are reported in ppm with reference to external samples of tetramethylsilane. Baseline corrections on the data were done in the Bruker TopSpin 4.2 software, and the ^{29}Si spectra were simulated and deconvoluted using the Voight line profile fitting in the Origin Pro software to quantify the alite and belite fractions.

Hydration, microstructure, and performance of plain and blended cements as a function of clinkering fuel.

The cement compositions used for the hydration, microstructure and performance studies are shown in Table 2. The anhydrous blends were homogenised in a roller ball mill using polymer balls to avoid further grinding. All samples were investigated at 0.5 w/c ratio. For characterising the microstructures, paste samples were prepared according to the procedure for mortars in EN 196-1 [32], but without aggregate. These were investigated for hydration kinetics, phase assemblages and pore structures using isothermal calorimetry, SEM, XRD, thermogravimetric analysis (TGA), mercury intrusion porosimetry (MIP) and dynamic vapour sorption (DVS).

Table 2 Composition of mixes investigated (%).

Constituent / Mix Id	CEM I 52.5 N (Ref)	CEM I 52.5 N (Net-zero mixed fuel)	GGBS (S)	Anhydrite
C_{NF}		100	-	-
C_{FF}	100	-	-	-
$C_{NF}S$	-	51	47	2
$C_{FF}S$	51	-	47	2

Isothermal calorimetry was used to assess the impact of the net zero fuel on hydration kinetics in plain and GGBS blended cements. Measurements were performed on 9 g of paste prepared at 0.5 w/b ratio using deionized water. The heat signal was corrected with quartz reference samples at the same water to solid ratio. The heat of reaction was monitored for 7 days in a TAM Air 8-channel calorimeter and the data presented in terms of the reaction rate and cumulative heat normalised by the mass of anhydrous cement.

Samples for XRD, SEM, TGA, MIP and DVS were cast into 15 ml plastic vials, sealed, and rotated on a low-speed planetary rotator for 12 hours to prevent bleeding. Still under sealed conditions, the

samples were stored in a water bath maintained at 20°C until hydration stoppage. After 1 and 28 days of hydration, specimens for XRD and TGA were crushed to pass 63 µm sieve, and hydration stopped using the double solvent removal technique [33]. Following the hydration stoppage, the samples were stored in mini-grip bags in a glovebox under a nitrogen atmosphere until they were tested.

The XRD data acquisition protocol described above for the anhydrous cement was used to scan the hydration-stopped samples after 1 and 28 days. The weight fractions of residual clinker phases were quantified and compared to the anhydrous for determining the degree of clinker hydration. Meanwhile, the Rietveld/PONKCS method, described in [33], was used to quantify the residual GGBS content and hence the degree of hydration of GGBS in $C_{NF}S$ and $C_{FF}S$. The control file was expanded to include crystallographic files for portlandite (ICSD #43433) [34], hemicarboaluminate (ICSD #263124) [35] monocarboaluminate (ICSD #59327) [36], hydrotalcite (ICSD #133742) [37], ettringite (ICSD #155395) [38] and a model for C-S-H based on the tobermorite structure of Richardson [39] for quantitative analyses of the hydrated phase assemblages, which were normalized per 100 g of the anhydrous binder.

The 28 days hydrated cement samples for SEM were 2 mm thick slices cut from the paste cylinders using a low-speed Isomet cutter. These were hydration stopped by soaking in isopropanol for 48 hours and rinsed in diethyl ether, resin impregnated and polished. Backscattered electron images, elemental mapping and point analyses were carried out to investigate the composition of the main reaction product, the calcium silicate hydrate (C-S-H) using the same SEM and data collection protocols described above for the clinker granules.

TGA data were acquired on a Netzsch thermal analyser 449 F5 Jupiter using platinum sample holders. For each measurement, about 25 mg of ground powder sample was heated at 20°C/min up to 1000°C in a nitrogen-purged atmosphere at a 60 ml/min gas flow rate. The mass change and its derivative were used to identify the water-rich hydrated phase assemblages. The bound water and portlandite contents were calculated between 50 and 550°C and ~ 400 – 500°C from the TGA curve using equations (1) and (2), respectively. The calculated weight fractions were normalised to the ignited weight at 1000°C.

$$W_n(\%) = \frac{\left(M_{50^\circ C} - M_{550^\circ C}\right)}{M_{550^\circ C}} * 100\ \%\text{----------} \quad (1)$$

$$CH(\%) = \frac{CH_{TG}\ {}^{74}/_{18}}{M_{550^\circ C}} * 100\ \% - - - - - - - - (2)$$

Where, W_n is the bound water in the sample, CH is the portlandite content; CH_{TG} is % weight loss from water associated with portlandite, calculated from the tangent method, $M_{50^\circ C}$ is the ignited weight at 50°C; $M_{550^\circ C}$ is the ignited weight at 550°C.

MIP measurements were performed on 1 – 2 mm crushed, and hydration stopped cement samples using a Quantachrome Instruments' PoreMaster-60. The data acquisition protocol and analysis are detailed elsewhere[40]. The MIP data are presented in terms of the cumulative intruded volume and the derivative.

A separate fraction of the crushed samples was used for DVS measurement on a nitrogen-purged Surface Measurement System DVS Resolution. The relative humidity (partial pressures) from 0–95–0 in 5% steps at 25°C with the time per step set to achieve equilibration at each step, using a dm/dt value of 0.002%/minute and a minimum step time and stability period of 10 minutes. Data was analysed using the SMS DVS Standard Analysis suite of Microsoft Excel macros to calculate an isotherm

from the raw data. The Isotherm Analysis suite was used to calculate the BET surface area. Other models used are the Dubinin-Radushkevich (DR), micropore analysis (t-plot) [41] and a modified Barrett, Joyner, and Halenda (BJH) model for mesopore analysis [42]. The micro and mesopore analysis calculations were based on a comparison with a non-porous reference material; this was obtained by running a sample of zirconium silicate under the same conditions as the hydrated cement samples. The DVS data is presented in terms of the micro and meso pore distribution after normalising the isotherms by the sample mass at 5% RH.

Mortar samples for compressive and flexural strength testing were 40x40x160 mm prisms, prepared at 1:3:0.5 binder to sand and water ratios according to EN196-1 [32] and tested after 1, 7 and 28 days. At each age, three prisms were tested for flexural strength and the resulting six halves were tested for compressive strength. The specimens for the 1-day strength were tested immediately after removal from the mould, while those for 7 and 28 days were cured in a water bath maintained at 20°C.

The phase assemblages formed as a function of time and degree of hydration of the cement clinker minerals and GGBS were verified by thermodynamic modelling using the GEMS Selektor v3 package. The thermodynamic data were taken from the PSI– Nagra [43] and Cemdata 18 [44] databases. The mineral composition of the cement as determined by QXRD and bulk composition of GGBS from XRF were used as inputs. Dissolution of the clinker minerals and GGBS as determined by QXRD/PONKCS were fitted using the empirical phase reaction model of Parrot and Killoh [45] with the coefficients adjusted as suggested in [46].

Results and discussion

The net zero fuel clinker and corresponding anhydrous CEM I

Figure 2a shows backscattered electron micrograph of the unground clinker and the overlayed elemental maps of sulphur, magnesium, iron, silicon, and aluminium is shown in Figure 2b. Granules of free lime were not observed, which is indicative of complete burning of the raw meal. The major clinker phases can be identified alongside variations in the grain sizes and textures of the calcium silicate phases while arcanite and periclase occupied the dark patches in the micrograph. However, the belite to alite contrast was less distinct than those reported in [47] where polished specimens were etched for observations under light microscope. Nevertheless, spherical and larger dendritic belite grains were evident from the overlayed elemental maps and were characterised by fine textured nodules, while the alite crystal's characteristic micro-cracks were noticed. Similarly textured belite, distinct from the lamellae crystals was reported elsewhere [48] and attributed to recrystallization reactions during polymorphic transitions and quenching of the clinkers [49]. The texturing of belite was also shown to be favoured at higher Al/Fe ratios [22]. Figure 2b further shows lower iron incorporation into the silicates such that the Al/Fe atomic ratio measured in the belites was ~3.6, being greater than the ratios reported in [22], where Al/Fe ratios were below 2.3, but the observation was comparable to average ratios reported in [50]. This implies that factors other than the Al/Fe ratio may explain the observed textures. Meanwhile, the interstitials nucleated at the silicate boundaries, as expected with the aluminates and ferrites distinguishable through the combined elemental maps.

The shapes and sizes of the calcium silicate minerals can reveal important information about the kiln temperature profile and potential fuel-raw meal interactions. The measured average grain sizes of alite ranged between 10 – 30 µm while belites were 15 – 40 µm, consistent with those reported in the literature [50]. The dendritic features could be due to dissolution of belites, probably constrained by limited lime for conversion into alite. The features found on the micrograph in Figure 2a and Figure 2b, therefore, highlight the specific effects of the fuel composition and temperature profile on the

clinker minerals, which bears significant implications on their grindability and subsequent reactivity of the cement.

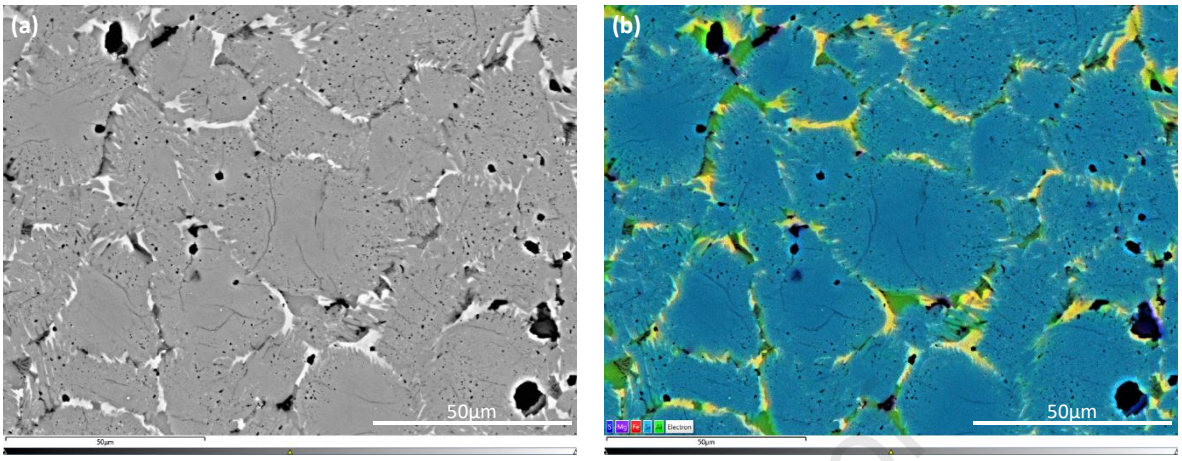

Figure 2 BSE images of the unground clinkers from the (a) net zero fuel and (b) overlayed elemental maps. Note: In (b), blue = sulphur, purple = magnesium, red = iron, light blue = silicon and green = aluminium.

Elemental compositions of the main clinker phases based on atomic ratios from EDS point analyses (shown in Table 3) offer further insight into the modifications which underpinned the polymorphic differences in the clinker. The reduction in alite's calcium concentration was balanced with sodium, potassium, and magnesium, while slightly more aluminium and phosphorous were incorporated into both alite and belite, which also contained lower iron than typically reported [50, 51]. These inclusions partly explain the observed texturing in the micrographs in Figure 2. The interstitials meanwhile showed a slight increase in the aluminium substitution by silicon and iron in the aluminate and ferrite phases. It was not possible to distinguish the aluminate polymorphs due to resolution of the EDS point analysis technique. However, the 8% and 42% substitution of calcium and aluminium respectively in the C_3A indicate a mixture of cubic and orthorhombic C_3A.

Table 3 stoichiometric composition of the major phases in the C_{NF} clinker based on the atomic ratios from EDS analysis.

Phase	Composition
C_3S	$(Ca_{0.85}Mg_{0.04}K_{0.01}Na_{0.01}Fe_{0.009})_3(Si_{0.9}Al_{0.04}P_{0.01}S_{0.04})O_{4.6}$
C_2S	$(Ca_{0.96}Mg_{0.016}K_{0.011}Na_{0.012})_2(Si_{0.9}Al_{0.062}Fe_{0.017}P_{0.003}S_{0.02})O_{3.8}$
C_3A	$(Ca_{2.76}K_{0.03}Na_{0.02}Mg_{0.2}Ti_{0.04})(Al_{0.96}Fe_{0.42}Si_{0.28})O_{5.86}$
C_4AF	$Ca_{2.03}Al_{0.98}Fe_{0.5}Mg_{0.17}Si_{0.25}Ti_{0.03}O_{4.7}$

The as-received C_{NF} sample and the corresponding enriched samples were analysed by XRD and NMR to examine the implications of the elemental variations on mineralogy. Figure 3a shows diffraction patterns of the enriched silicate minerals and the enriched interstitial in Figure 3b, focused on the relevant angular windows to reveal characteristic peaks and the effect of minor inclusions. X-ray reflections denoting the major clinker phases can be identified, albeit with some structural modifications evident from the peak shapes, particularly the intensity ratios of the primary *hkl* reflections. The doublet reflections between 32 – 33° 2θ in Figure 3a indicate the monoclinic form of alite but, the overlap with belite in the $(60\bar{6})$ and (224) reflection ranges causes uncertainties in the

polymorph assignment. The relative intensity ratio between the $(60\bar{6})$ and (224) reflections was much greater while the ratio between the (14.24) and (040) reflections observed between 51 – 52.5° 2θ exceeded unity. These indicate a mixture of the M_1 and M_3 alite polymorphs [50, 52], consistent with the presence of periclase in Figure 3b and the EDS composition in Table 3, which showed higher magnesium incorporation in alite. Structure search and match on the data confirmed dominance of the M_3 alite with small levels of the M_1 polymorphs. The refined lattice parameters of these matched closely the structures of De La Torre *et al.* [53] and de Noirfontaine *et al.* [54] respectively. This implies that the alite polymorphs formed in the C_{NF} clinker conformed to those typical in industrial cements.

Variations in the belite polymorphs in the C_{NF} clinker were also evident from Figure 3a. Assigning XRD peaks to belite in industrial cement is not straightforward due to the substantial overlap with alite in the same 2θ range. However, high-temperature XRD data [50] and synthetic belite doped with phosphorous [17] or boron [55] help to identify the belite polymorphs. From Figure 3a, the *hkl* reflections at (611) and (031) represent α'_H-C_2S while those at (120) and $(12\bar{1})$ represent β-C_2S, thus indicative of the co-existence of the α'_H and β-C_2S polymorphs in the C_{NF} clinker. The former plausibly arose from the higher levels of MBM, which, together with hydrogen and glycerine, replaced coal as fuel. From Figure 3b, the C_3A polymorph and C_4AF were unaffected by the net zero fuel; cubic C_3A (440) with some orthorhombic C_3A (224) were observed while the *hkl* reflections at $(200, 14\bar{1})$ and (002) denoted the C_4AF phase. Notably, the C_3A/C_4AF intensity ratio was more significant in the net zero fuel than typically reported in the literature, suggesting a lower ferrite phase consistent with the EDS maps and elemental ratios in Table 3.

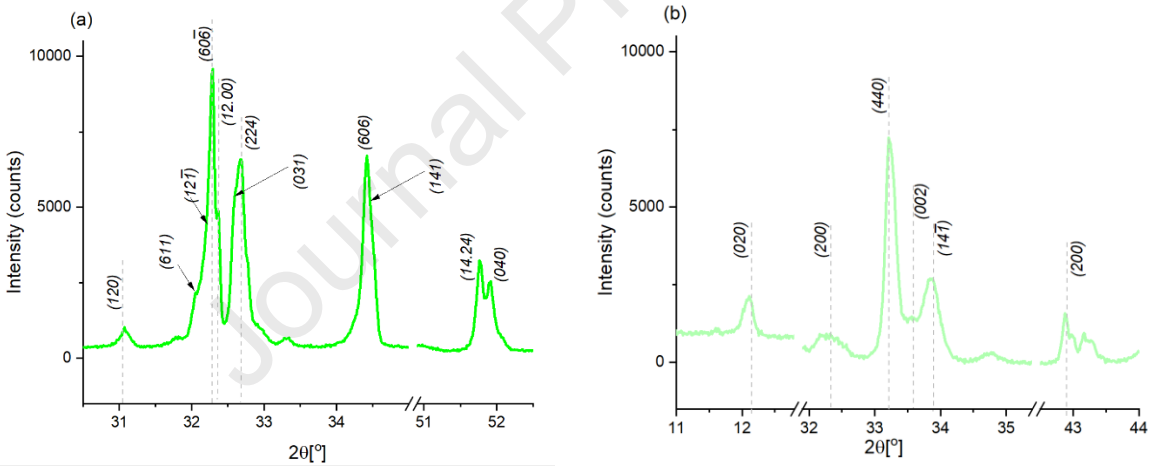

Figure 3 XRD trace of the selectively enriched C_{NF} cement: (a) silicate phases after dissolving in the KOH/sucrose solution (b) interstitials after dissolving in salicylic acid/methanol solutions using the methods of Guttridge [31].

The clinker content and ratios between the main phases are important quality indicators of cement performance. From the results in Table 4, the total clinker content in the plain cement was 90% while the minor additional constituents comprising a mixture of anhydrite, bassanite, calcite and periclase constituted 10%. Of the clinker content, alite and belite made up 80% at 3:1 alite/belite ratio, which is slightly lower compared to typical industrial cement. The α'_H-C_2S polymorph constituted 55% of the total belite content, while the β-C_2S polymorph was approximately 45%. Occurrence of the α'_H-C_2S is noteworthy given its faster reaction than β-C_2S [23, 55]. Whether the temperature profile or the fuel composition dictated the observed belite polymorphs is uncertain. However, according to the literature, α'_H-C_2S which forms at higher temperature than β-C_2S (i.e. >1160°C) is stabilized at room temperature through partial substitution of silicon by phosphorous [16] which can be expected with

the MBM in the fuel. Increasing the phosphorous concentration was directly correlated with the stabilization of belite over alite [18] and α'_H-C_2S, at higher phosphorous and iron concentrations in the raw meal [17]. It is noteworthy that limited α'_H-C_2S formed in clinkers doped with <1.1% P_2O_5 but excess phosphate also hindered α'_H-C_2S formation and retarded hydration of belite-rich cement [16]. Optimisation of the phosphorous concentration in the fuel and hence the biofuel content is therefore essential to maintain the acceptable alite and α'_H-C_2S contents in the clinker.

Cubic C_3A existed alongside the orthorhombic type, consistent with the 6.5% alkalis including magnesium in the aluminate structure as revealed by the EDS results in Table 3. The overall levels of both C_3A and C_4AF were in line with the levels in commercial cements and not modified significantly by the investigated fuel.

Table 4 Mineralogical composition of the C_{NF} cement based on quantitative XRD.

Mixes / Phase	C_3S	α'_H-C_2S	β-C_2S	C_3A_{cub}	C_3A_{orth}	C_4AF	Anhydrite	Basanite	Calcite	Periclase
C_{NF}	56.4	9.8	8.3	4.3	2.9	7.1	3.6	0.6	4.8	1.4

To evaluate the chemical environments of alumina incorporated into the minerals, ^{27}Al NMR scans were performed on the as-received cement, enriched silicate and interstitial samples and the results shown in Figure 4. Two central transitions between 50 – 100 ppm and -20 – 20 ppm denoting tetrahedral (Al(IV)) and octahedral (Al(VI)) coordinated aluminium respectively are noticed. The deshielded centre-band at 96 ppm and the main singular peak at 79 ppm plus various sub-peaks characterised the tetrahedral coordinated aluminium, indicative of some Al^{3+} partially substituting Si^{4+} in belite and alite. The octahedral coordinated aluminium showed a symmetrical centre band at -20 to 20 ppm centred at ~-0.6 ppm, coinciding with that of the interstitials and amplified in the enriched interstitials sample. This implies that another aluminium site, likely to be X-ray amorphous, co-existed in the clinker with similar coordination in the silicates and interstitials, being more concentrated in the latter. The tetrahedral centre band at ~56 ppm was unique to the enriched interstitial sample and distinct from previously reported C_3A centre-bands at around 80 ppm. The lower frequency shift in the Al(IV) of the interstitial sample therefore indicates greater electron density around the aluminium nucleus compared to those substituted for the silicate minerals. This shielding is consistent with the extent of ion substitution, especially silicon in the interstitials as revealed by EDS (Table 3).

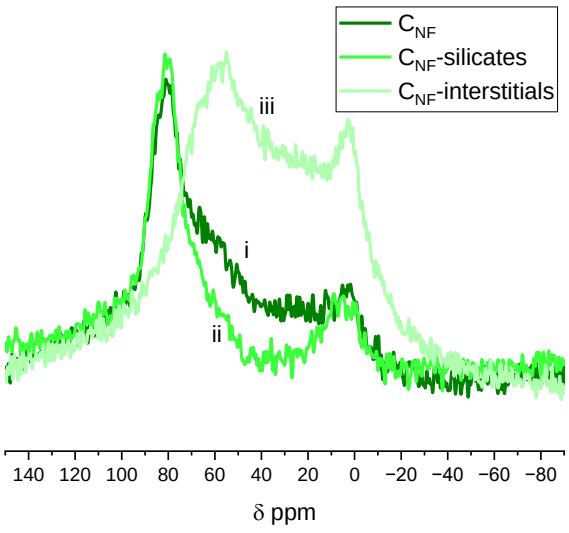

Figure 4 ^{27}Al NMR spectrum (9.4 T, 20 kHz, 16,384 scans) showing central transition for Al ions in the (i) as received cement, enriched (ii) silicates and (iii) interstitials in the C_{NF}cement and after selective enrichment of the silicates and interstitial phases.

358

359 The impact of the net zero kiln fuel on the chemical environment of aluminium could only be evaluated
360 qualitatively owing to the spectral resolution. The Al(VI)/Al(IV) intensity ratios of the silicates were
361 greater, indicative of lower Al substitution in the silicates as observed from the EDS-derived
362 stoichiometric compositions (Table 3). Some studies have shown that increasing sulphate
363 incorporation into the silicate phases also raised the aluminium concentration [57], which can
364 ultimately impede the reaction of the silicate phases [58].

365 Meanwhile, the ^{29}Si NMR spectra (Figure 5) reveal distinctive information about the silicon
366 coordination in the as-received clinker, which closely matched the enriched silicate spectra. Silicon
367 ions incorporated into the interstitial phases were not detectable at the resolution of the acquired
368 data. Simulation of the enriched silicate spectra allowed a closer examination of the calcium silicates.
369 These were characterised by a well-resolved resonance at -71.4 ppm corresponding to belite, but
370 polymorphs could not be differentiated from the single resonance. The overlapping resonances in the
371 -78 to -66 ppm range are attributable to alite, whose sub-spectra comprised broad resonances at ~-
372 70.4, -73.6 and -75.5 ppm, typical of the M_3 alite polymorph. The diffused resolution of the alite sub-
373 spectra indicates ion substitution [59], consistent with the elemental composition in Table 3.
374 Moreover, the peak area ratio of belite/alite was 0.36, combined with the bulk SiO_2 from XRF, and the
375 elemental composition (Table 3) yields 55.4% and 16.2% alite and belite, respectively. These are within
376 the typical ranges reported for OPC [50, 59, 60] and show excellent agreement with the quantitative
377 XRD alite and belite contents in Table 4.

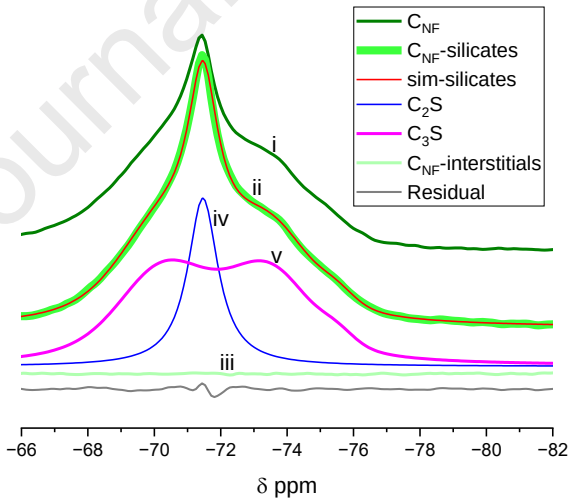

Figure 5 ^{29}Si NMR (9.4 T, 6 kHz, 2048 scans) spectra of the as received clinker (i) enriched calcium silicates (ii) and the interstitial (iii) phases alongside the optimized simulation (trace on the silicates) and deconvoluted belite (iv) and alite (v) phases C_{NF} cement and after selective enrichment of the silicates and interstitial phases.

378

379 The results presented above on the clinkers and the cements have shown polymorphic differences in
380 the alite and belite phases and their relative contents. The EDS analyses also confirmed more
381 magnesium and phosphorous but less sulphur, aluminium, and iron substitution in the C_{NF} clinker.
382 Moderate variations in the raw meal and volatiles in the kiln (i.e., pre-existing or emanating from the
383 fuels), fuel ashes or the lack of these, plus the kiln temperature profile, might have contributed to the
384 polymorphic changes in the main phases. For example, hydrogen being more combustible than coal

and MBM can cause a sharper heating gradient [10], exposing the raw meal faster to the high-temperature range due to the shorter ignition distance than that typically encountered in coal-rich kiln fuels. The endothermic reactions involved in the formation of belite, and the interstitials plausibly extended the belite formation temperature range further, consuming quicklime, and modifying the overall belite concentration. Therefore, the limiting step in the fraction of alite quantified in Table 4, which is lower than the levels in some commercial cements, may be due to the depletion of quicklime in the stabilized α'_H-C_2S rather than the attained temperature range for the fuel mix. Moreover, alternative fuels' combustion can also reduce the oxygen and sulphur concentrations in the kiln [10] and, their incorporation in the clinker phases, which potentially contributed to the observed polymorphs and the alite/belite ratio in the C_{NF} clinker.

Hydration kinetics and microstructure

The preceding sections revealed a moderately lower alite/belite ratio and significantly higher α'_H-C_2S in the C_{NF} clinker and cement. Evaluating the hydration kinetics and microstructures formed in cements based on this clinker is imperative to understanding their performance.

Figure 6a shows the isothermal heat of reaction measured up to 7 days in the plain and blended GGBS cements from the net zero fuel clinker (C_{NF} and $C_{NF}S$) compared to the reference cements (C_{FF} and $C_{FF}S$). Moderate differences in the kinetics of the silicate and aluminate reactions as a function of the clinkering fuel were evident. A shorter induction time and an intense main reaction peak characterised C_{NF} and $C_{NF}S$ compared to the C_{FF} equivalent. However, slopes of the acceleration stage reactions leading to the main silicate peak were comparable between the plain cements, C_{NF} and C_{FF}, with the peak reached after about 9 hours. The aluminate reaction/sulphate depletion peak, observed as a shoulder on the silicate peak was less noticeable in the C_{NF} sample, seemingly merged with the silicate peak. This occurred after ~15 hours in the reference sample, suggesting potential differences in the sulphate/alumina consumption in the plain cements.

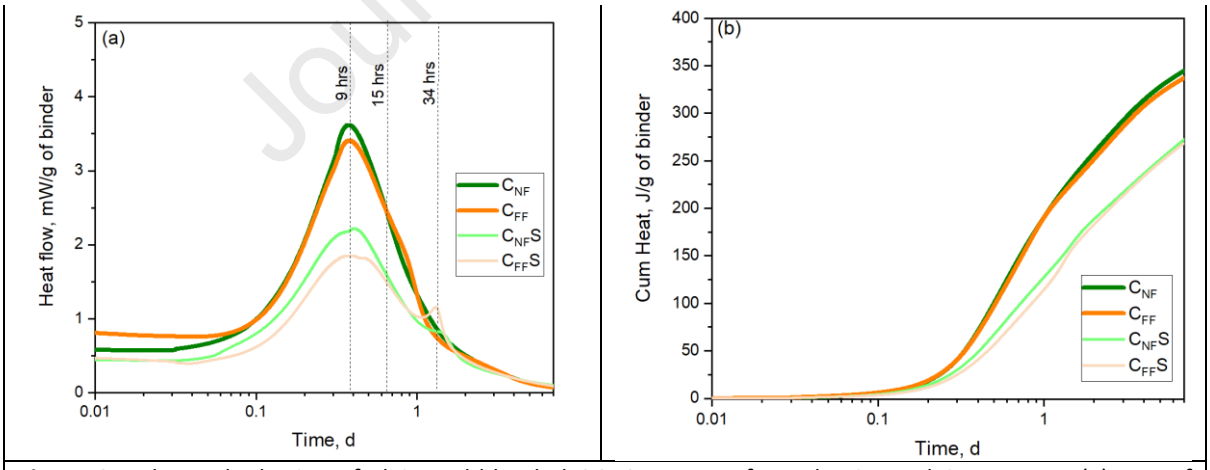

Figure 6 Early age hydration of plain and blended GGBS cements from the C_{NF} and C_{FF} cements (a) rate of reaction (b) cumulative heat as measured by isothermal calorimetry.

The blended cements, $C_{NF}S$ and $C_{FF}S$ showed a lower rate of reaction due to the 50% reduction in the clinker factor, although with similar features as the plain cements. The silicate reaction was enhanced in $C_{NF}S$, but the time to the main reaction peaks was not modified significantly by the clinkering fuel type nor the presence of GGBS. However, the aluminate peaks showed some differences despite

comparable SO_3 contents in the cements (see Table 1). The first aluminate peak occurred 3 hours faster in $C_{NF}S$ compared to $C_{FF}S$, but the second aluminate peaks were delayed in both blended cements until ~34 hours. The higher surface area and fineness of C_{NF} may explain the greater silicate and aluminate reactions in the corresponding plain and blended cement, while the higher sulphate content in the blended cements (see Figure 7) explains the delayed second aluminate peaks in $C_{NF}S$ and $C_{FF}S$.

The kinetic differences notwithstanding, the cumulative heat (Figure 6b) shows marginally high total heat in the C_{NF} than the reference C_{FF} and the $C_{NF}S$ than $C_{FF}S$. Moderately elevated alkali content, plus lower iron [17] and aluminium [58] incorporated into the C_{NF} clinker, possibly accelerated and enhanced the silicates hydration. Moreover, a faster reaction of the α'_H-C_2S could also contribute to the marginal increase in cumulative heat in C_{NF} and $C_{NF}S$ than the reference equivalents.

QXRD/PONKCS analysis was used to follow the hydration reactions and products with a view to elucidating the contributory factors underpinning the above calorimetry data. Comparisons between the QXRD/PONKCS results and the thermodynamic modelling of C_{NF} and $C_{NF}S$ are shown in Figure 7a and Figure 7b respectively. The residual clinker minerals and GGBS determined from QXRD/PONKCS analyses were fitted reasonably by the modified phase dissolution model of Parrot and Killoh [45, 46]. These were implemented in GEMS, providing a basis to predict the stable phase assemblages, assuming equilibrium in the dissolved and precipitated species. In the early hours of hydration (<~3 hours), alkalis and sulphates dissolve rapidly alongside a gradual alite consumption. After that, alite dissolved faster. This point corresponded to the onset of the acceleration stage of hydration (Figure 6a) with increased precipitation of C-S-H, portlandite and hydrogarnet predicted (Figure 7a and 7b). Ettringite precipitated alongside these, but its content plateaued once anhydrite was dissolved fully. The time to complete anhydrite dissolution reflected the sulphate balance in the cements. After 1 day, the degree of hydration of alite was 55 – 65% in mixes C_{NF} and $C_{NF}S$, respectively, reaching 90 – 98% by 28 days. Meanwhile, 19 – 22% degree of hydration of belite was measured after 1 day and increased to 50 – 60% after 28 days. While the measured and modelled degree of hydration of alite was expected, that of belite was significantly higher than typically reported [52, 61], but the data is consistent with the polymorphs identified in the C_{NF} clinker.

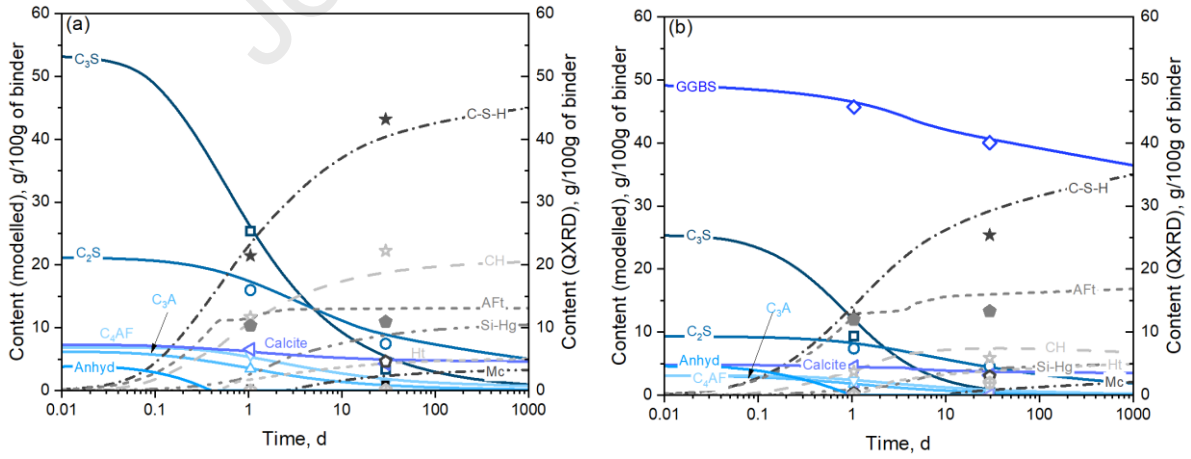

Figure 7 Predicted phase assemblages as a function of the dissolution kinetics of (a) the clinker minerals in the C_{NF} cement and (b) with GGBS in the $C_{NF}S$ cement over the course of hydration. The solid lines denote the modelled dissolution kinetics of the anhydrous minerals, GGBS and anhydrite. The dashed lines represent the predicted phase assemblages in in GEMS. The phase contents of the anhydrous and phase assemblages calculated from QXRD/PONCKS are shown as scatter points after 1 and 28 days.

445 *Microstructure*

446 The thermodynamic modelling results in Figure 7 (a and b) predicted the C-S-H, ettringite, portlandite
447 and silicious hydrogarnet as the main hydrated assemblages with some monocarboaluminate and
448 hydrotalcite. The quantities of these depended on the binder composition and degree of hydration.
449 The predicted phase assemblages were verified experimentally through SEM, TGA and XRD.

450 Figure 8 (a – d) shows backscattered SEM micrographs of the hydrated cement pastes after 28 days.
451 These reveal an intermix of hydration products, unreacted clinker, GGBS, and capillary pores. Light
452 grey assemblages denoting portlandite were uniformly interspersed within the C-S-H phases and more
453 dominant in the plain cement, C_{NF} and C_{FF}.

454 The hydrated plain cement showed fewer grains of unreacted clinker phases in sample C_{NF} (Figure 8a)
455 compared to C_{FF} (Figure 8b). In the latter, partially reacted grains with contrasts of bright phases,
456 corresponding to an intermix of belite and ferrite, can be noticed. In the GGBS blends (Figures 8c and
457 8d), traces of unreacted clinker, especially the bright ferrite phases and GGBS grains, can be identified
458 alongside relicts of the reacted GGBS. Differences in the capillary porosity of the pastes can also be
459 identified in the micrographs, being more dominant in the blended cements. The reference C_{FF} and
460 $C_{FF}S$ cements showed larger capillary pores than the corresponding C_{NF} and $C_{NF}S$ samples. These
461 observations are consistent with the anhydrous cement particle size distribution (Figure 1) and the
462 reaction kinetics (Figure 6 and Figure 7).

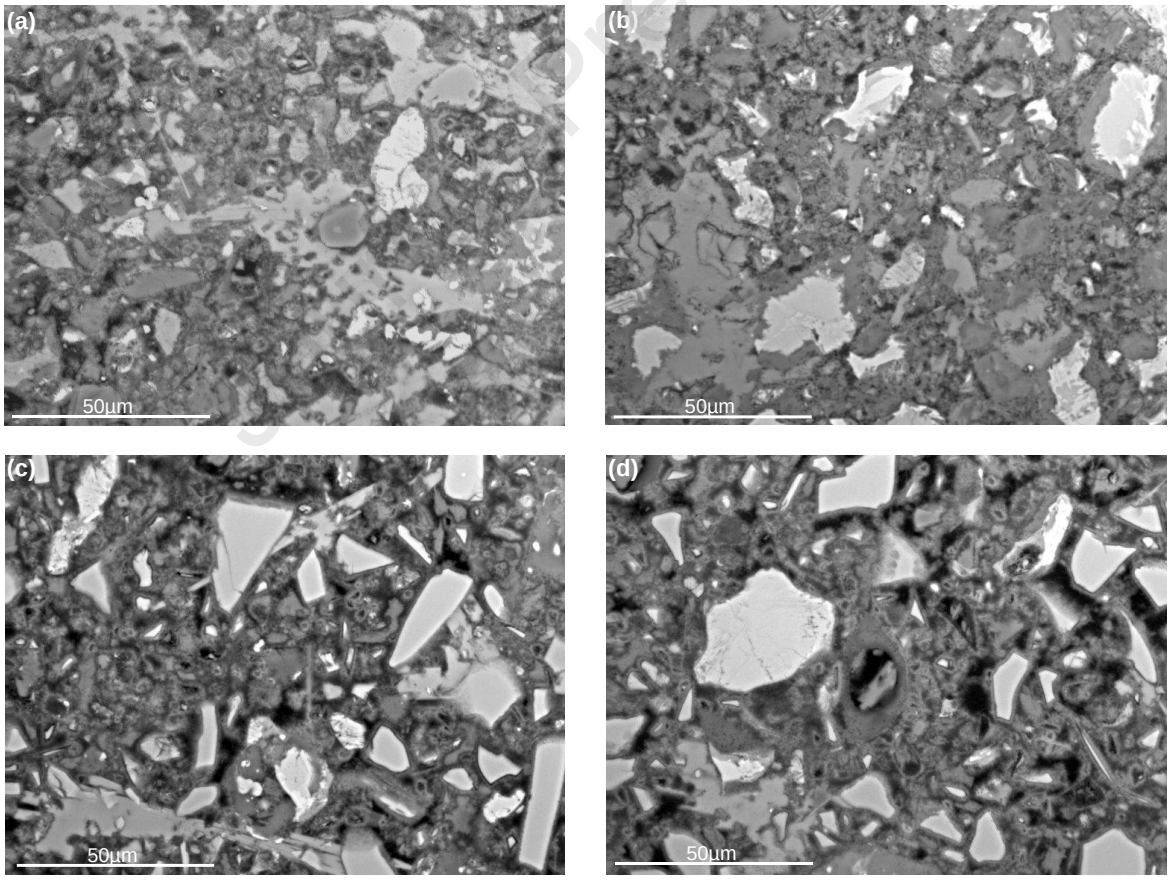

Figure 8 Backscattered electron micrographs showing types and distribution of phase assemblages in plain and blended GGBS cements from C_{NF} compared to their C_{FF} equivalent, measured by SEM: (a) C_{NF} (b) C_{FF} (c) $C_{NF}S$ and (d) $C_{FF}S$ after 28 days of hydration.

463

The TGA/DTG spectra in Figure 9 measured on 28-day samples confirmed C-S-H and ettringite, carboaluminates, hydrotalcite and portlandite as the main hydration products. Calcite in the hydrated C_{NF} samples is residual from the limestone added as a minor additional constituent (MAC, see Table 4). The C-S-H and ettringite endotherms were comparable in the plain cements, but slightly more portlandite can be observed in C_{NF}. Comparison of the plain and blended cement endotherms suggest more C-S-H and or ettringite in the blended cement. Both products consume calcium and reduce the portlandite content with the lower clinker factor. Meanwhile, endotherms of carboaluminates (marked as Hc/Mc) were noticed in all samples but were dominant in the C_{NF} and $C_{NF}S$ samples due to the excess limestone from the MAC. The TGA calculation inserted in Figure 9 indicates higher bound water and portlandite contents in the plain C_{NF} cement, which agrees with the kinetics data in Figure 6 and Figure 7. The portlandite contents in $C_{NF}S$ and $C_{FF}S$ are consistent with the enhanced clinker hydration in the cements (see Figure 7). However, the TGA-measured portlandite content was much lower in $C_{NF}S$ than $C_{FF}S$. The higher degree of hydration of clinker, would be expected to contribute more portlandite, yet a lower content was measured in $C_{NF}S$. This indicates greater portlandite consumption in $C_{NF}S$, which agrees with the degree of GGBS reaction in Figure 7 and the bound water contents (insert in Figure 9).

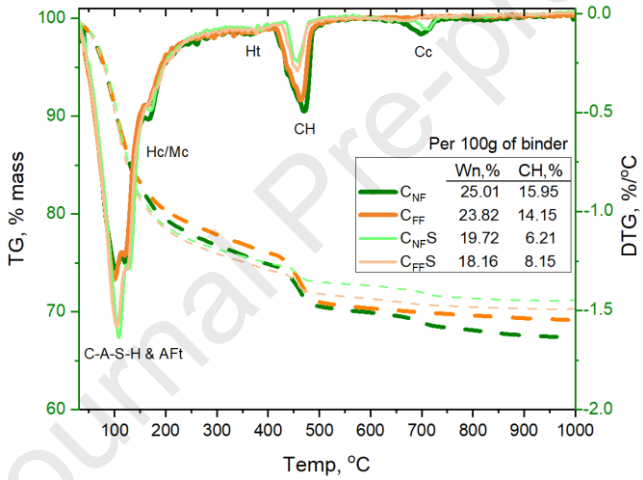

Figure 9 TGA/DTG plots showing the thermal decomposition of the main water-rich phase assemblages in the C_{NF} plain and blended cements compared to C_{FF} equivalents measured after 28 days of hydration.

In Figure 10a, XRD patterns of the anhydrous and hydrated pastes focused in the 8 – 35° 2θ range to reveal the crystalline and semi-crystalline phase assemblages along with the clinker minerals are presented. These confirm the C-S-H, portlandite and ettringite as the primary assemblages in the plain and blended cements by 1 day, and after 28 days, carboaluminates and hydrotalcite can be observed. The observations confirm the phase assemblages predicted by the thermodynamic modelling in Figure 7 (a and b). The exception is hydrogarnet. Due to its weak XRD reflection and overlap with the C-S-H, distinct peaks corresponding to the latter could not be assigned. Calcite from limestone in C_{NF} stabilized ettringite in the plain and blended cement. Slightly more calcium sulphate in the blended cement retarded calcite dissolution and hence carboaluminate precipitation. In the 28d samples, hemi and monocarboaluminate reflections were identified in $C_{NF}S$ but only monocarboaluminate in C_{NF}, plausibly due to the limited aluminium availability after the interstitial aluminate depletion.

Quantitative analyses of the XRD data, showing the unreacted clinker minerals, GGBS and phase assemblages formed, plus the calculated degree of hydration of clinker and GGBS are presented in

Figure 10b. Between 1 and 28 days, more portlandite and C-S-H were calculated in both cements, consistent with the dissolution kinetics (Figure 7 a and b) and the bound water (Figure 9). Compared to C_{NF}, the $C_{NF}S$ sample showed more ettringite due to the elevated sulphate but less portlandite and C-S-H due to the lower clinker factor and overall degree of hydration respectively. Comparison between the QXRD results and those predicted in GEMS can be seen in Figure 7 (a and b). Consistency between the datasets is remarkable, except hydrogarnet that was not quantified in the analysis and significantly lower C-S-H in the $C_{NF}S$ samples. Given that hydrogarnet was not quantified, one would expect more C-S-H calculated. It seems the underestimation was at the expense of the residual GGBS calculation by PONKCS, which may imply possibly greater degree of GGBS hydration than calculated.

These results demonstrate that the main hydrates were not affected by the clinkering fuel, but the volume of formed phase assemblages and their evolution with time were modified due to reactivity of the minerals and the MAC in the cement. Stabilization of Hc/MC over ettringite at 28 days and portlandite consumption to form C-S-H and Hc/Mc are well-known phenomena in plain and blended cement due to the additionally dissolved alumina from GGBS [62] and their interactions with dissolved anionic species [63].

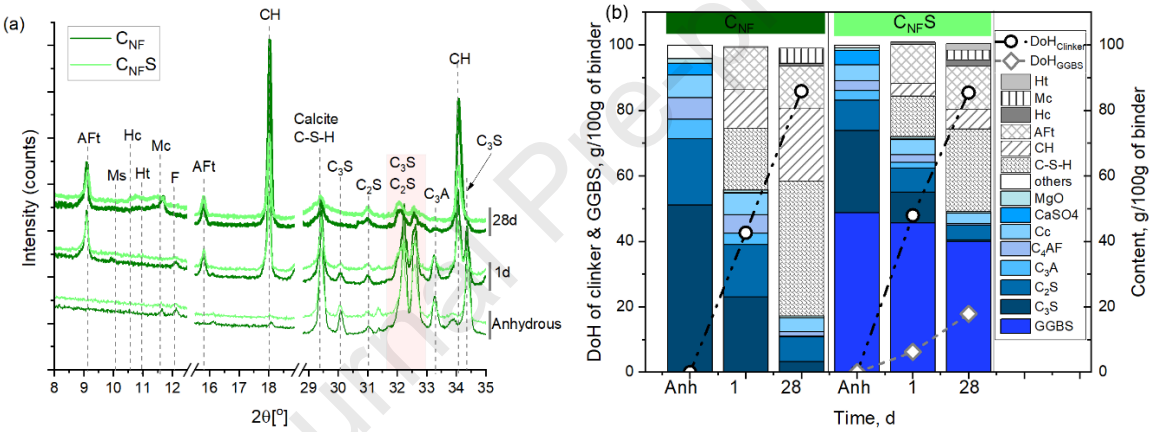

Figure 10 XRD data showing (a) diffraction trace of anhydrous and hydrated C_{NF} and $C_{NF}S$ cements, focused to reveal the main minerals and crystalline phase assemblages and (b) quantitative XRD analysis of the anhydrous cements and pastes after 1- and 28-days hydration. In (a), the bottom set is the trace for anhydrous cements, middle set is hydrated paste after 1-day and top set is hydrated pastes after 28-days. Note, the offsets in the vertical axis of (a) are for clarity. In (b), the degree of hydration of the clinker minerals was calculated for C_{NF} and $C_{NF}S$ and GGBS in $C_{NF}S$. There is ±2% margin of error associated with the degree of hydration calculated.

The composition of the C-S-H phase from the plain and blended cements plotted in terms of the Al/Ca versus Si/Ca based on EDS atomic ratios are shown in Figure 11, together with tabulated Ca/Si and Al/Ca ratios. Note, the Ca/Si ratio was calculated as the reciprocal of the furthest point cluster on the Si/Ca axis while the slope, drawn from the origin through the lowest points on the Al/Ca axis was taken as the Al/Si ratio according to [39]. Whereas the C-S-H Ca/Si and Al/Si differed between the plain and blended cements, the effect of the clinkering fuel on these was moderate, and the ranges are consistent with the literature on GGBS blended cements [62]. The $C_{NF}S$ and $C_{FF}S$ cements' lower C-S-H Ca/Si ratio is due to a lower calcium content in the GGBS compared to plain cement and the subsequent calcium consumption to form additional hydration products. Meanwhile, elevated alumina in the pore solutions due to GGBS hydration tends to increase the C-S-H Al/Si as in the alite

and belite. Consequently, the clinkering fuel had no measurable effect on the composition of the C-S-H phase in the plain or blended cements.

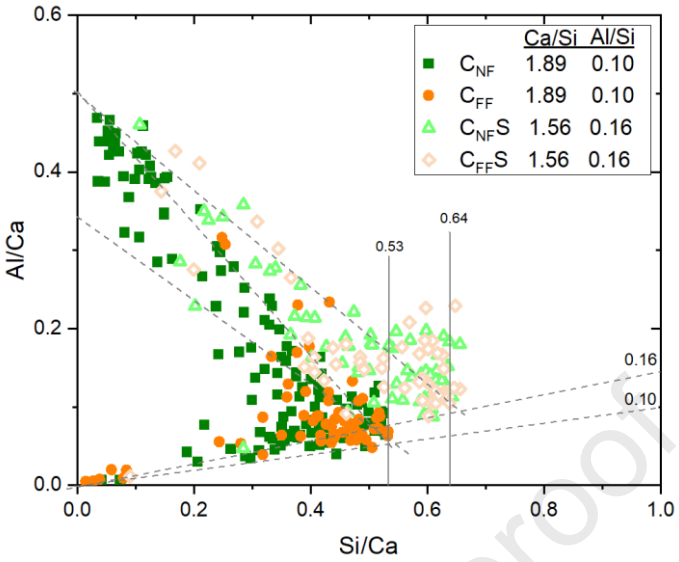

Figure 11 SEM/EDS of the outer product C-A-S-H in the plain and blended GGBS cements based on C_{NF} compared to C_{FF} equivalent after 28 days hydration.

The C-S-H compositional similarity notwithstanding, differences in the reaction kinetics and volume of hydrates affected the pore distribution and porosity. The mercury intruded porosity and its derivative (Figure 12a) showed three pore clusters ranging between 5 – 20 nm, 20 – 100 nm and > 100 nm, corresponding to the meso, micro-capillary and macro-capillary pores. It must be noted that the MIP technique does not resolve pores finer than 4 nm, which dominate the gel and the C-S-H interlayers [64]. In the MIP accessible pore ranges, the clinkering fuel had a negligible effect on the crossover between the meso and capillary pores. The micro-capillary pores were densified in $C_{NF}S$ and $C_{FF}S$, but macro-pores also existed in the corresponding plain cements. For each cement category, however, the C_{FF} cement showed greater porosity than the C_{NF} equivalent, but the critical pore size diameters were not modified considerably. Meanwhile, the DVS data (Figure 12b) gave further insight into the mesopore ranges that were inaccessible by MIP.

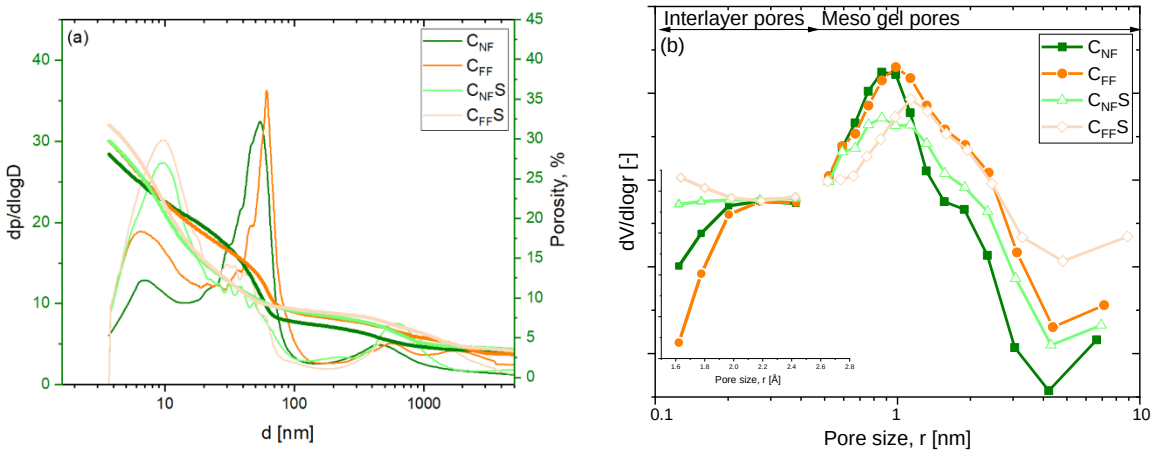

Figure 12 Pore structure of the investigated plain and blended GGBS cement based on C_{NF} and C_{FF} cements. (a) differential and cumulative intruded volume plots from MIP and (b) distribution of micro (insert in 12b) and meso pore distribution calculated from the desorption isotherm as measured by DVS.

The interlayer pores (insert in Figure 12b) corresponding to the C-S-H interlayer spaces showed slight coarsening in the blended cement. However, adsorption causes swelling and collapse in these pore ranges during the measurement, and hence, it is uncertain whether the aluminium incorporation in the blended cement influenced the trends since the latter were much denser, below ~1 nm. Above this, the C_{NF} and $C_{NF}S$ samples showed a smaller volume of finer pores than the C_{FF} equivalent. These observations can be explained by the pore refinement arising from the additionally formed hydration products, as revealed by the degree of hydration and weight fraction of hydrates evident from Figure 9 and Figure 10 respectively.

Compressive strength

Figures 13(a and b) show compressive and flexural strength of mortars prepared from the investigated plain cements (C_{NF} and C_{FF}), and their corresponding GGBS blends ($C_{NF}S$ and $C_{FF}S$) measured after 1, 7 and 28 days. Higher compressive strength was measured in the C_{NF} mortars compared to the C_{FF} equivalent, although the difference reduced with time, falling within the measurement error by 28 days. As expected, compressive strength evolved slowly in the blended GGBS mixes, which were still lower than the corresponding plain cement mixes after 28 days. This is consistent with results from strength tests based on similar GGBS [65] and can be explained by the slow reactivity of GGBS compared to cement clinker (see Figure 10b). Unlike the plain cement mortars, differences in compressive strength of $C_{NF}S$ and $C_{FF}S$ mortars were within the measurement error, suggesting a negligible influence of the investigated net zero fuel on the strength of blended cement mortars, except at early age when the latter was up to 5 MPa greater. Meanwhile, flexural strength development in the mortars followed similar trends as the compressive strength, comparable between C_{NF} and C_{FF} cement whether plain or blended. The strength profiles are consistent with the kinetics and microstructure studies, which identified slightly improved reactivity and densified pore structures in C_{NF} and $C_{NF}S$ cements compared to their fossil fuel equivalent under the same testing conditions.

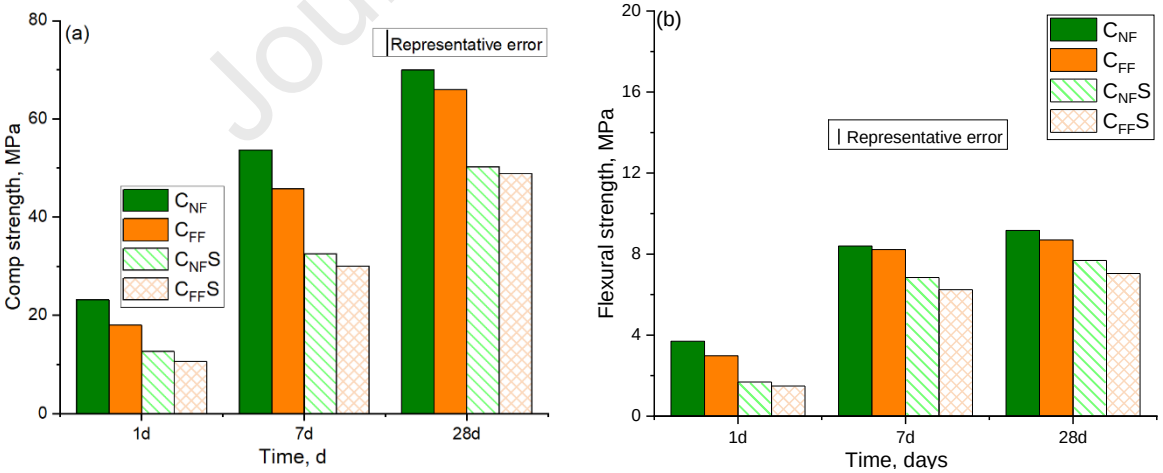

Figure 13 Strength evolution in the investigated plain and blended GGBS cement based on clinkers from net zero and reference. (a) compressive and (b) flexural strength monitored up to 28 days.

Conclusions and recommendations

This study investigated representative clinker and cement from a net zero-emission fuel that comprised mixed hydrogen, MBM and glycerine used in an industrial cement plant. The hydration, microstructures, and performance of plain and blended cement from the clinker were compared with commercial grade fossil fuel equivalent. Based on the results and discussion, the following conclusions are drawn:

a. The four main minerals - alite, belite, calcium aluminate and calcium alumino-ferrite phases were identified in the net zero fuel clinker although with polymorphic differences prominent in the belite phase. The alite/belite ratio (~3) was slightly lower compared to typical fossil fuel-derived industrial cement clinkers, but the α'_H-C_2S polymorph was also found in the net zero fuel clinker which constituted about 55% of the total belite content.
b. Tetrahedral aluminium coordination (i.e. Al(IV)) in the net zero fuel interstitials was more shielded and pivoted at ~56 ppm compared to 80 ppm reported for Portland cement C_3A and 81 – 96 ppm denoting Al(IV) incorporated into alite and belite. Guest ions including silicon in the interstitial phases led to the shielding. Moreover, the octahedrally coordinated aluminium site, likely to be an X-ray amorphous phase concentrated more in the interstitials.
c. The net zero fuel cement's alite and belite reacted faster and attained an overall greater degree of reaction than the levels reported for fossil fuel produced cement in the literature. The kinetic effects arose from the M_3 alite and α'_H-C_2S polymorphs, which reacted faster and contributed additional reaction products as reflected in the bound water contents.
d. The nature of reaction products including composition of the C-S-H phase, portlandite, ettringite and carboaluminates was not modified significantly by the clinkering fuel, except for the volume of hydrates in the plain and blended cements. The increased kinetics and volume of reaction products reduced porosity compared to the fossil fuel equivalent cements and led to slightly improved strength at the investigated timescales.

The observed polymorphic differences, reaction kinetics and microstructures indicate that the trial cement/clinker fulfils the market requirements, demonstrating a comparable performance to the reference cement. Implementation of hydrogen-based net zero fuels for cement clinker production at an industrial scale is therefore feasible. However, kinetics of combustion of the different fuel substitutes and possible interactions with the raw meal may require optimisation before deploying at scale.

Acknowledgement: The authors acknowledge access to the characterisation facilities at the UKCRIC National Centre for Infrastructure Materials at the University of Leeds (EPSRC grant no. EP/P017169/1)

Credit authorship:

Samuel Adu-Amankwah: Conceptualization, Investigation, Data curation, Supervision, Resources, Formal analysis, Writing – drafting, review & editing. **Ben Douglas:** Methodology, Formal analysis, writing – review & editing. **Leslie Arkless**: Methodology, Formal analysis, writing – review & editing. **Nina Cardinal:** Funding, writing – review & editing. **Maciej Zajac:** Conceptualization, Methodology, Resources, Writing – review & editing.

References

[1] J.S. Damtoft, J. Lukasik, D. Herfort, D. Sorrentino, E.M. Gartner, Sustainable development and climate change initiatives, Cement and Concrete Research 38(2) (2008) 115-127.
[2] L. Barcelo, J. Kline, G. Walenta, E. Gartner, Cement and carbon emissions, Materials and Structures 47(6) (2014) 1055-1065.

606 [3] E. Gartner, H. Hirao, A review of alternative approaches to the reduction of CO2 emissions
607 associated with the manufacture of the binder phase in concrete, Cement and Concrete Research 78
608 (2015) 126-142.
609 [4] K.L. Scrivener, V.M. John, E.M. Gartner, Eco-efficient cements: Potential economically viable
610 solutions for a low-CO2 cement-based materials industry, Cement and Concrete Research 114 (2018)
611 2-26.
612 [5] A. Chatterjee, T. Sui, Alternative fuels – Effects on clinker process and properties, Cement and
613 Concrete Research 123 (2019) 105777.
614 [6] J. Skocek, M. Zajac, M.J.S.R. Ben Haha, Carbon Capture and Utilization by mineralization of
615 cement pastes derived from recycled concrete, 10(1) (2020) 1-12.
616 [7] T. Proske, S. Hainer, M. Rezvani, C.-A. Graubner, Eco-friendly concretes with reduced water and
617 cement contents — Mix design principles and laboratory tests, Cement and Concrete Research 51
618 (2013) 38-46.
619 [8] CEMBUREAU, 2050 Carbon Neutrality Roadmap, 2020.
620 [9] H.-M. Ludwig, W. Zhang, Research review of cement clinker chemistry, Cement and Concrete
621 Research 78 (2015) 24-37.
622 [10] J. Hercog, R. Lewtak, B. Glot, P. Jóźwiak, G. Nehring, V.D. Tavares, A.M. Nunes, D. Gaspar, Pilot
623 testing and numerical simulations of the multifuel burner for the cement kiln, Fuel 342 (2023)
624 127801.
625 [11] C. Pieper, B. Liedmann, S. Wirtz, V. Scherer, N. Bodendiek, S. Schaefer, Interaction of the
626 combustion of refuse derived fuel with the clinker bed in rotary cement kilns: A numerical study,
627 Fuel 266 (2020) 117048.
628 [12] A. Rahman, M.G. Rasul, M.M.K. Khan, S. Sharma, Recent development on the uses of alternative
629 fuels in cement manufacturing process, Fuel 145 (2015) 84-99.
630 [13] I.A. Altun, Influence of heating rate on the burning of cement clinker, Cement and Concrete
631 Research 29(4) (1999) 599-602.
632 [14] M. Ichikawa, M. Kanaya, Effects of minor components and heating rates on hte fine textures of
633 alite in Portland cement clinker, Cement and Concrete Research 27(7) (1997) 1123-1129.
634 [15] N. Husillos Rodríguez, S. Martínez-Ramírez, M.T. Blanco-Varela, S. Donatello, M. Guillem, J. Puig,
635 C. Fos, E. Larrotcha, J. Flores, The effect of using thermally dried sewage sludge as an alternative fuel
636 on Portland cement clinker production, Journal of Cleaner Production 52 (2013) 94-102.
637 [16] A. Diouri, A. Boukhari, J. Aride, F. Puertas, T. Vázquez, Elaboration of α'L-C2S form of belite in
638 phosphatic clinker. Study of hydraulic activity, Materiales de Construcción 48(249) (1998) 23-32.
639 [17] M.Y. Benarchid, A. Diouri, A. Boukhari, J. Aride, I. Elkhadiri, Hydration of iron–phosphorus doped
640 dicalcium silicate phase, Materials Chemistry and Physics 94(2) (2005) 190-194.
641 [18] T. Staněk, P. Sulovský, The influence of phosphorous pentoxide on the phase composition and
642 formation of Portland clinker, Materials Characterization 60(7) (2009) 749-755.
643 [19] F. Puertas, M.T. Blanco-Varela, Use of alternative fuels in cement manufacture. Effect on clinker
644 and cement characteristics and properties, Materiales de Construcción 54(274) (2004) 51-64.
645 [20] K. Serrano-González, A. Reyes-Valdez, O. Chowaniec, Impact of the use of alternative fuels on
646 clinker reactivity, Materiales de Construcción 67(326) (2017) e120.
647 [21] T. Staněk, P. Sulovský, The influence of the alite polymorphism on the strength of the Portland
648 cement, Cement and Concrete Research 32(7) (2002) 1169-1175.
649 [22] K. Fukuda, I. Maki, S. Ito, H. Yoshida, C. Kato, Effect of Al/Fe Ratio in Belite on the Microtexture
650 Induced by the Remelting Reaction, J. American Ceramic Society 77(11) (1994) 3027-3029.
651 [23] T. Link, F. Bellmann, H.M. Ludwig, M. Ben Haha, Reactivity and phase composition of Ca2SiO4
652 binders made by annealing of alpha-dicalcium silicate hydrate, Cement and Concrete Research 67
653 (2015) 131-137.
654 [24] C.-J. Winter, Hydrogen energy — Abundant, efficient, clean: A debate over the energy-system-
655 of-change, International Journal of Hydrogen Energy 34(14, Supplement 1) (2009) S1-S52.

[25] S. Sharma, S.K. Ghoshal, Hydrogen the future transportation fuel: From production to applications, Renewable and Sustainable Energy Reviews 43 (2015) 1151-1158.
[26] M. Ozturk, I. Dincer, Utilization of waste heat from cement plant to generate hydrogen and blend it with natural gas, International Journal of Hydrogen Energy 47(48) (2022) 20695-20704.
[27] R.S. El-Emam, K.S. Gabriel, Synergizing hydrogen and cement industries for Canada's climate plan – case study, Energy Sources, Part A: Recovery, Utilization, and Environmental Effects 43(23) (2021) 3151-3165.
[28] F.B. Juangsa, A.S. Cezeliano, P.S. Darmanto, M. Aziz, Thermodynamic analysis of hydrogen utilization as alternative fuel in cement production, South African Journal of Chemical Engineering 42 (2022) 23-31.
[29] MPA, State of the art fuel mix for UK cement production to test the path for 'Net Zero': A technical, environmental and safety demonstration https://assets.publishing.service.gov.uk/government/uploads/system/uploads/attachment_data/file/1119898/phase_3_state_of_the_art_fuel_mix_for_UK_cement_production_to_test_the_path_for_net_zero.pdf, 2022.
[30] W. Ariyaratne, M. Melaaen, K. Eine, L. Tokheim, Meat and bone meal as a renewable energy source in cement kilns: Investigation of optimum feeding rate, International conference on renewable energies and power quality, Spain, 2010, pp. 1244-1249.
[31] W.A. Gutteridge, On the dissolution of the interstitial phases in Portland cement, Cement and Concrete Research 9(3) (1979) 319-324.
[32] BSI, EN 196-1:2016 Methods of testing cement. Determination of strength, 2016.
[33] S. Adu-Amankwah, M. Zajac, P. Hou, L. Black, Impact of hydration stoppage on quantification of the GGBS content in ternary limestone cements using the PONKCS method, Materials and Structures 56(6) (2023) 113.
[34] D.M. Henderson, H.S. Gutowsky, A nuclear magnetic resonance determination of the hydrogen positions in Ca(OH)21, American Mineralogist 47(11-12) (1962) 1231-1251.
[35] T. Runcevski, R.E. Dinnebier, O.V. Magdysyuk, H. Pollmann, Crystal structures of calcium hemicarboaluminate and carbonated calcium hemicarboaluminate from synchrotron powder diffraction data, Acta Crystallographica Section B 68(5) (2012) 493-500.
[36] M. Francois, G. Renaudin, O. Evrard, A Cementitious Compound with Composition 3CaO.Al2O3.CaCO3.11H2O, Acta Crystallographica Section C 54(9) (1998) 1214-1217.
[37] E.S. Zhitova, S.V. Krivovichev, I. Pekov, H.C. Greenwell, Crystal chemistry of natural layered double hydroxides. 5. Single-crystal structure refinement of hydrotalcite, [Mg6Al2(OH)16](CO3)(H2O)4, Mineralogical Magazine 83(2) (2019) 269-280.
[38] F. Goetz-Neunhoeffer, J. Neubauer, Refined ettringite (Ca6Al2(SO4)3(OH)12·26H2O) structure for quantitative X-ray diffraction analysis, Powder Diffraction 21(1) (2006) 4-11.
[39] I.G. Richardson, The calcium silicate hydrates, Cement and Concrete Research 38(2) (2008) 137-158.
[40] S. Adu-Amankwah, M. Zajac, C. Stabler, B. Lothenbach, L. Black, Influence of limestone on the hydration of ternary slag cements, Cement and Concrete Research 100 (2017) 96-109.
[41] M.M. Dubinin, Physical Adsorption of Gases and Vapors in Micropores, in: D.A. Cadenhead, J.F. Danielli, M.D. Rosenberg (Eds.), Progress in Surface and Membrane Science, Elsevier1975, pp. 1-70.
[42] E.P. Barrett, L.G. Joyner, P.P. Halenda, The Determination of Pore Volume and Area Distributions in Porous Substances. I. Computations from Nitrogen Isotherms, Journal of the American Chemical Society 73(1) (1951) 373-380.
[43] T. Thoenen, D.J.V. Kulik, Switzerland: Paul Scherrer Institut, Nagra/PSI chemical thermodynamic data base 01/01 for the GEM-Selektor (V. 2-PSI) Geochemical Modeling Code: Release 28-02-03, (2003).
[44] B. Lothenbach, D.A. Kulik, T. Matschei, M. Balonis, L. Baquerizo, B. Dilnesa, G.D. Miron, R.J. Myers, Cemdata18: A chemical thermodynamic database for hydrated Portland cements and alkali-activated materials, Cement and Concrete Research 115 (2019) 472-506.

[45] L.J. Parrot, D.C. Killoh, Prediction of cement hydration, Proceedings of the British Ceramic Society, 1984, pp. 41-53.
[46] B. Lothenbach, F. Winnefeld, Thermodynamic modelling of the hydration of Portland cement, Cement and Concrete Research 36(2) (2006) 209-226.
[47] I. Maki, S. Ito, T. Tanioka, Y. Ohno, K. Fukuda, Clinker grindability and textures of alite and belite, Cement and Concrete Research 23(5) (1993) 1078-1084.
[48] K. Masaki, I. Maki, Effect of prolonged heating at elevated temperatures on the phase composition and textures of portland cement clinker, Cement and Concrete Research 32(6) (2002) 931-934.
[49] K. Fukuda, Recent Progress in Crystal Chemistry of Belite: Intracrystalline Microtextures Induced by Phase Transformations and Application of Remelting Reaction to Improvement of Hydration Reactivity, Journal of the Ceramic Society of Japan 109(1267) (2001) S43-S48.
[50] H.F.W. Taylor, Cement Chemistry, 2nd ed., Thomas Telford1997.
[51] G. Le Saoût, V. Kocaba, K. Scrivener, Application of the Rietveld method to the analysis of anhydrous cement, Cement and Concrete Research 41(2) (2011) 133-148.
[52] G. Le Saout, T. Füllmann, V. Kocaba, K. Scrivener, Quantitative study of cementitious materials by X-ray diffraction/Rietveld analysis using an external standard, Proceedings of the 12th International Congress on the Chemistry of Cement, Montréal, QC, Canada, 2007, pp. 8-13.
[53] Á.G. De La Torre, S. Bruque, J. Campo, M.A.G. Aranda, The superstructure of C3S from synchrotron and neutron powder diffraction and its role in quantitative phase analyses, Cement and Concrete Research 32(9) (2002) 1347-1356.
[54] M.N. de Noirfontaine, M. Courtial, F. Dunstetter, G. Gasecki, M. Signes-Frehel, Tricalcium silicate Ca3SiO5 superstructure analysis: a route towards the structure of the M1 polymorph, 227(2) (2012) 102-112.
[55] A. Cuesta, E.R. Losilla, M.A.G. Aranda, J. Sanz, Á.G. De la Torre, Reactive belite stabilization mechanisms by boron-bearing dopants, Cement and Concrete Research 42(4) (2012) 598-606.
[56] S. Boughanmi, I. Labidi, A. Megriche, H. Tiss, A. Nonat, Does phosphorus affect the industrial Portland cement reactivity?, Construction and Building Materials 188 (2018) 599-606.
[57] T. Staněk, P. Sulovský, Active low-energy belite cement, Cement and Concrete Research 68 (2015) 203-210.
[58] F. Begarin, S. Garrault, A. Nonat, L. Nicoleau, Hydration of alite containing aluminium, Advances in Applied Ceramics 110(3) (2011) 127-130.
[59] J. Skibsted, H.J. Jakobsen, C. Hall, Quantification of calcium silicate phases in Portland cements by 29Si MAS NMR spectroscopy, Journal of the Chemical Society, Faraday Transactions 91(24) (1995) 4423-4430.
[60] S.L. Poulsen, V. Kocaba, G. Le Saoût, H.J. Jakobsen, K.L. Scrivener, J. Skibsted, Improved quantification of alite and belite in anhydrous Portland cements by 29Si MAS NMR: Effects of paramagnetic ions, Solid State Nuclear Magnetic Resonance 36(1) (2009) 32-44.
[61] S. Shirani, A. Cuesta, A. Morales-Cantero, A.G. De la Torre, M.P. Olbinado, M.A.G. Aranda, Influence of curing temperature on belite cement hydration: A comparative study with Portland cement, Cement and Concrete Research 147 (2021) 106499.
[62] M. Whittaker, M. Zajac, M. Ben Haha, F. Bullergahn, L. Black, The role of the alumina content of slag, plus the presence of additional sulfate on the hydration and microstructure of Portland cement-slag blends, Cement and Concrete Research 66 (2014) 91-101.
[63] S. Adu-Amankwah, L. Black, L. Xianfeng, P. Hou, M. Zajac, Early age reaction of slag in composite cement: Impact of sulphates and calcite, CEMENT 14 (2023) 100085.
[64] A.C.A. Muller, K.L. Scrivener, A reassessment of mercury intrusion porosimetry by comparison with 1H NMR relaxometry, Cement and Concrete Research 100 (2017) 350-360.
[65] S. Adu-Amankwah, S.A. Bernal Lopez, L. Black, Influence of component fineness on hydration and strength development in ternary slag-limestone cements, RILEM Technical Letters 4(0) (2019) 81-88.

Highlights

1. Cement clinker produced from net zero fuel comprising mixed hydrogen and biofuels in industrial plant is reported.
2. Significant quantities of α'- C_2S form alongside C_3S, β-C_2S, C_3A and C_4AF in the clinker.
3. Kinetics of reaction of the net zero fuel clinker are faster than fossil fuel equivalent.
4. Densified pore structures improved compressive and tensile strength.

Declaration of interests

The authors have no competing interests to declare.